Splitter plate effect on the global dynamics of two-phase mixing layer flow

Original
Splitter plate effect on the global dynamics of two-phase mixing layer flow / Vecchiè, Salvatore; Della Pia, Alessandro. - In: INTERNATIONAL JOURNAL OF MULTIPHASE FLOW. - ISSN 0301-9322. - 193:(2025). [10.1016/j.ijmultiphaseflow.2025.105370]

Availability:
This version is available at: 20.500.11771/38198

Publisher:

Published
DOI:10.1016/j.ijmultiphaseflow.2025.105370

Splitter plate effect on the global dynamics of two-phase mixing layer flow

Salvatore Vecchiè[1,2] and Alessandro Della Pia*[2]

[1]Università degli Studi di Napoli “Federico II”, Naples, 80125, Italy
[2]Modelling and Engineering Risk and Complexity, Scuola Superiore Meridionale,,
School for Advanced Studies, Naples, 80128, Italy

August 7, 2025

Abstract

We combine two-dimensional volume-of-fluid direct numerical simulation (2D-VOF) and dynamic mode decomposition analysis (DMD) to investigate the splitter plate thickness effect on the global dynamics of a planar two-phase mixing layer. The flow configuration consists of two parallel fluid streams with different densities ($\rho_1 < \rho_2$) and velocities ($U_1 > U_2$), which meet downstream of a separator (splitter) plate. The interaction between the fast (U_1) and slow (U_2) fluid layers determines a Kelvin-Helmholtz (KH) instability at the interface, which is found to be crucially affected by the parameter e/δ_1, being e the splitter plate thickness and δ_1 the vorticity thickness of the fast phase (placed above the slow phase). For $e/\delta_1 < 1$, the KH instability results in a wavy dynamics of the interface, whose temporal oscillations are characterized by the reduced frequency $St_{ML} = f\delta_1/U_1 \approx 0.018$. In such conditions, the DMD analysis identifies the dominant global mode of the flow as a spatio-temporal interfacial travelling wave moving with the celebrated Dimotakis velocity, $U_D = \sqrt{\rho_1}U_1 + \sqrt{\rho_2}U_2/\left(\sqrt{\rho_1} + \sqrt{\rho_2}\right)$, and oscillating at the same frequency St_{ML}. On the other hand, for $e/\delta_1 > 1$, the reduced frequency

---

*Corresponding author: `a.dellapia@ssmeridionale.it`

of the interface oscillations undergoes a sudden transition (shift) to the lower value $St_{ML}^{W} \approx 0.012$. The leading spatio-temporal coherent structure identified by the DMD analysis correspondingly shifts to the same frequency. By inspection of the velocity field, it is found that, as e/δ_1 increases, the wake region located right downstream of the splitter plate undergoes a transition from steady conditions to periodic oscillations at the reduced frequency $St^{W} \approx 0.024$. Therefore, it is argued that the observed frequency shift in the mixing layer global dynamics is determined by the interaction between the characteristic frequencies of the wake $\left(St^{W}\right)$ and the mixing layer (St_{ML}), resulting in the third-order intermodulation frequency $St_{ML}^{W} = 2St_{ML} - St^{W}$, which is known to arise for wave signals propagating in nonlinear systems potentially. We corroborate this argument by applying a simple actuation at the splitter plate edge, which inhibits the wake oscillations and restores the frequency St_{ML} even in the $e/\delta_1 > 1$ regime, thereby suppressing the frequency shift.

1 Introduction

Two-phase mixing layer flows have been a matter of active research in fluid dynamics for centuries [1, 2]. Technical and industrial applications of such flow configurations span a multitude of engineering sectors, including automotive [4], ocean [5], aerospace [3] and naval [6] engineering, and have motivated extensive theoretical, numerical, and experimental studies over the years.

The common thread overall in applications is the physical setup, involving the interaction between a relatively low-speed liquid jet (density ρ_2, velocity U_2) and a faster co-flowing fluid phase (density ρ_1, velocity U_1) downstream of a splitter plate, which initially separates the two streams (see Fig. 1 in the following Section 2). The velocity difference between the fast (upper) and slow (lower) phases triggers a shear instability at the separating interface, leading to the generation of an interfacial wave traveling with the celebrated Dimotakis velocity $U_D = \sqrt{\rho_1}U_1 + \sqrt{\rho_2}U_2 / \left(\sqrt{\rho_1} + \sqrt{\rho_2}\right)$ [7]. The wave dynamics are further characterized by secondary instabilities, determining the formation, corrugation, and finally breaking of ligaments into droplets (primary atomization). The resulting droplet mixtures then mutually interact in the so-called secondary atomization process [8]. In this study, we are concerned with the early stages of the primary instability occurring at the two-fluid interface right after the splitter plate edge (near-field region), and in particular with the effect of the plate thickness on the global dynamics of the mixing layer flow. Understanding the physical mechanisms that lead to the development of instabilities in the near-field region is critical, due to its significant impact on the development of the turbulent flow field in the downstream region [9].

The interfacial wave dynamics in the proximity of the splitter plate have been conventionally investigated through linear stability analysis of small perturbations superposed on a properly selected base flow, within the parallel (or quasi-parallel) flow approximation, to determine the most unstable frequency and wavelength of the instability. First investigations were carried out assuming an inviscid regime for both the base flow and the evolution of perturbations, and neglecting the splitter plate effect [8, 10]. Later on, Matas *et al.* [11] included a velocity defect in the base flow, to mimic the splitter plate effect on the near-field flow region. They found that accounting for the velocity defect is crucial to obtain reasonable quantitative agreement between inviscid stability analysis predictions and experimental measurements of the interface oscillations frequency, although the spatial growth rate of the travelling wave was significantly underestimated. On the other hand, a good quantitative match between measured and theoretically predicted spatial growth rates can be obtained by including viscous effects in the temporal linear stability analysis, but then frequencies become overestimated [12, 13].

To obtain a more satisfactory and systematic agreement between stability analysis predictions and experimental measurements, Otto *et al.* [14] developed a spatio-temporal linear stability approach, improving the match between theoretical and experimental values for both frequency and spatial growth rate. Moreover, their method provided for the first time evidence of a transition from convective to absolute instability [15], for the injection conditions reported in the work by Matas *et al.* [11], with experimental data spanning both the instability regimes. This aspect was further clarified by Fuster *et al.* [16], who showed that the transition from convectively to absolutely unstable behaviour of the flow crucially depends on the dynamic pressure ratio parameter $M = \rho_1 U_1^2/(\rho_2 U_2^2)$. In particular, the absolute instability regime was found to be strongly affected by the splitter plate thickness separating the two streams before the injection.

Later on, Bozonnet *et al.* [17] pointed out that such absolute instability is determined by a resonance mechanism between an upstream-travelling surface capillary wave and the main downstream-oriented shear wave. In this respect, Matas *et al.* [18] outlined that surface tension is the physical mechanism triggering the flow absolute instability for a sufficiently low interfacial velocity. Moreover, Matas [19] found that the finite thicknesses of the fluid streams may play a key role in triggering the absolute instability, through the so-called confinement effect.

As explained in the more general framework of jet/wake flows by Juniper [20, 21] and retrieved for an air-water mixing layer configuration in the analysis by Bozonnet *et al.* [17], confinement is indeed able to determine absolute instability. This is possible through a resonance mechanism taking place between velocity perturbations cross-stream spatial oscillations within the fast phase, which are induced by the streamwise interfacial wave development, and the confinement length (i.e. the fast stream injection thickness H_1). While both the convective mode of instability (triggered by viscosity differences across the interface [13]) and the surface tension-induced absolute mode [16] are characterized by relatively small wavelengths, the confinement absolute mode reveals a smaller wave number, which better matches most of the experimental conditions [22, 23]. A map of the different mixing layer flow regimes has been recently proposed by Matas *et al.* [18], outlining that the velocity defect induced in the near-field region by the splitter plate has an impact on both the surface tension and confinement-induced absolute instability.

From the literature review summarized above, it arises that two-phase mixing layers instability mechanisms have been mostly investigated through local stability analyses, namely selecting the velocity profiles at certain representative locations of the (base) flow (estimated by means of theoretical arguments or measured with numerical simulations and experiments) and computing the most unstable frequencies and wavelengths by means of temporal/spatio-temporal linear stability approaches. Numerical simulations performed both in three-dimensional [9] and two-dimensional [16, 17] scenarios have shown that such flows are characterized by strong spatial variations in the near-field region. The locally parallel flow assumption, usually made for linear stability calculations, therefore generally does not hold. As pointed out by Bozonnet *et al.* [17], a global stability analysis has to be performed to improve the predictions of mixing layer flows dynamics in most of the conditions of interest.

Motivated by such considerations, the purpose of this work is to investigate the global dynamics of two-phase mixing layer flows by combining two-dimensional volume-of-fluid direct numerical simulation (2D-VOF) and data-driven global stability analysis based on dynamic mode decomposition (DMD). In particular, we aim at shedding light on the effect of the splitter plate thickness e on the dominant mode of the flow instability, which is identified as a spatio-temporal coherent structure associated to a global oscillation frequency.

This investigation is inspired by the works by Fuster *et al.* [16] and Ben Rayana *et al.* [24, 25], who provided numerical and experimental measurements of the local oscillation frequency at the interface for a number of e values. By means of the local analysis, these authors found a shift of the flow dominant oscillation frequency when the parameter e increases beyond a critical threshold, opening up a question regarding the driving mechanisms underlying this phenomenon. As stated in Fuster *et al.* [16], *"it is difficult to conclude whether the dynamics of the contact line is responsible for the frequency shift or not... We therefore believe that the frequency shift is a consequence of the flow created behind the separator plate and not of the contact line dynamics. In any case, this phenomenon certainly requires further investigations in the future."*

The problem is addressed here by providing systematic numerical simulations of the two-phase mixing layer flow, spanning both the $e/\delta_1 < 1$ and $e/\delta_1 > 1$ regimes identified by Fuster *et al.* [16], δ_1 being the vorticity thickness of the fast fluid stream shearing the slow phase. By applying dynamic mode decomposition to the numerical data, the variation of flow structures and associated global oscillation frequencies are monitored as the splitter plate thickness changes, ultimately allowing for the identification of the physical mechanisms responsible for the frequency shift.

The rest of the work is organized as follows. In Section 2, we introduce the flow configuration of interest. In Section 3, we describe the numerical methodologies employed in the analysis. Results are presented in Section 4, and conclusions are provided in Section 5.

2 Physical layout

The planar two-phase mixing layer flow configuration of interest is schematically represented in Fig. 1. A slow fluid stream with velocity U_2 is placed below a fast stream with velocity U_1. The two streams have finite thicknesses H_1 and H_2, respectively, and they meet downstream of a splitter plate with thickness equal to e. The domain is a two-dimensional (2D) square focused

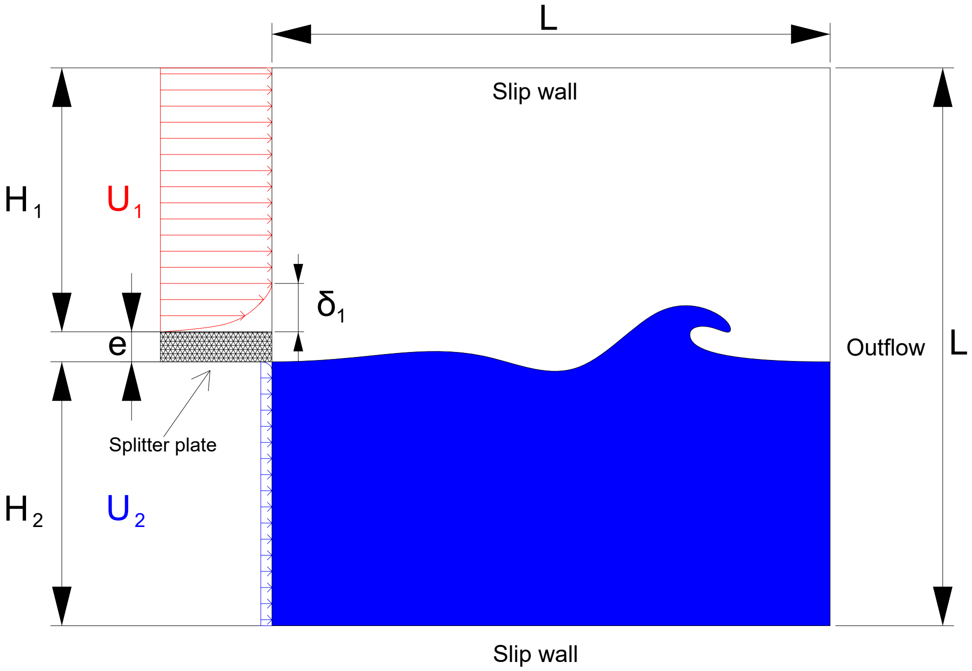

Figure 1: Schematic representation of the computational domain, including the employed boundary conditions and a sketch of the two-phase mixing layer interfacial wave.

around the plate. The velocity field is defined as $\mathbf{u} = (u, v)$, where u, v are the velocity components in the x and y directions, respectively, with $0 \leq x \leq L$ and $0 \leq y \leq L$, and $L = H_1 + e + H_2$. The origin $\mathcal{O}$ of the reference frame $\mathcal{O}xy$ coincides with the bottom left corner of the domain.

The choice of a 2D computational framework is justified by the 2D nature of the interfacial instability developing downstream of the splitter plate, which is not affected by three-dimensional transverse modulations in the near-field flow region of interest ([16, 22, 25]). Moreover, we choose not to include the splitter plate separating the fluid streams in the computational domain, but to mimic its effect via boundary conditions. As reported in the recent work by Bozonnet *et al.* [17], this choice allows for avoidance of the simulation of the contact line dynamics on the plate, which is expensive given its typical scales, and to directly enforce the shape of the inflow velocity profile. This is assigned on the left side of the computational domain as

$$u(y) = \begin{cases} U_2, & 0 \leq y \leq H_2, \\ 0, & H_2 < y \leq H_2 + e, \\ U_1 \cdot \operatorname{erf}\left(\dfrac{y - H_2 - e}{\delta_1}\right), & H_2 + e < y \leq H_2 + e + H_1, \end{cases} \tag{1}$$

while $v = 0$ for $0 \leq y \leq L$. The volume fraction C is prescribed as $C = 1$ for $0 \leq y \leq H_2$, and as $C = 0$ for $y > H_2$. Following previous works ([9, 16, 17]), the error function

$$\operatorname{erf}(y) = \frac{2}{\sqrt{\pi}} \int_0^y \exp(-\chi^2)\, d\chi, \tag{2}$$

is employed to represent the vorticity layer on the bottom boundary of the fast stream, whose thickness is denoted as δ_1. The remaining boundary conditions are enforced as follows: on top and bottom sides of the domain, homogeneous Neumann conditions are prescribed for all variables except v, which is assigned equal to $v = 0$ (slip condition), while a standard outflow condition

$$\frac{\partial u}{\partial x} = \frac{\partial v}{\partial x} = \frac{\partial C}{\partial x} = 0, \quad p = 0, \tag{3}$$

is considered on the right boundary, allowing for the convection of interfacial waves without artificial reflection. The initial conditions are prescribed as $u = v = C = p = 0$ in the whole domain.

The computational domain is discretized employing a uniform mesh with $N_x = N_y = 2^8$ grid points along each spatial dimension, corresponding to a mesh size equal to $\Delta \approx \delta_1/12$. Note that a resolution of $\Delta = \delta_1/10$ has been recently shown to be adequate in accurately capturing the two-phase mixing layer flow interfacial dynamics [17]. The simulation time-step is evaluated at each iteration as

$$\Delta T = \min\left(\frac{0.5\Delta}{u}, \sqrt{\frac{\rho_1 + \rho_2}{2}\frac{\Delta^3}{\pi\gamma}}\right), \tag{4}$$

which is the minimum value between the CFL-based time-step and the oscillation period of the smallest capillary wave that can be captured by the grid, being γ in Eq. (4), the surface tension coefficient. Further details on the numerical simulations are provided in the following Section 3.1, while the grid convergence analysis of results presented in Section 4 is reported in A.

Name	Variable	Value	Unit
Fast stream density	ρ_1	100	Kg m^{-3}
Slow stream density	ρ_2	1000	Kg m^{-3}
Fast stream viscosity	μ_1	0.001	Kg m^{-1} s^{-1}
Slow stream viscosity	μ_2	0.1	Kg m^{-1} s^{-1}
Inlet fast stream velocity	U_1	10	m s^{-1}
Inlet slow stream velocity	U_2	1.0	m s^{-1}
Inlet fast stream thickness	H_1	0.010	m
Inlet slow stream thickness	H_2	0.010	m
Surface tension coefficient	γ	0.1	N m^{-1}
Fast stream vorticity thickness	δ_1	0.001	m
Splitter plate thickness	e	$[0.5, 1.5] \cdot 10^{-3}$	m

Table 1: Dimensional quantities involved in the problem. Note that the splitter plate thickness e is the only parameter varied in the analysis.

Name	Relation	Value
Density ratio	$r_\rho = \rho_1/\rho_2$	0.1
Viscosity ratio	$r_\mu = \mu_1/\mu_2$	0.01
Reynolds number	$Re = \rho_1 U_1 \delta_1/\mu_1$	1000
Weber number	$We = \rho_1 U_1^2 \delta_1/\gamma$	100
Dynamic pressure ratio	$M = \rho_1 U_1^2/(\rho_2 U_2^2)$	10
Plate-to-thickness ratio	e/δ_1	[0.5, 1.5]

Table 2: Main dimensionless parameters corresponding to the physical quantities listed in Table 1.

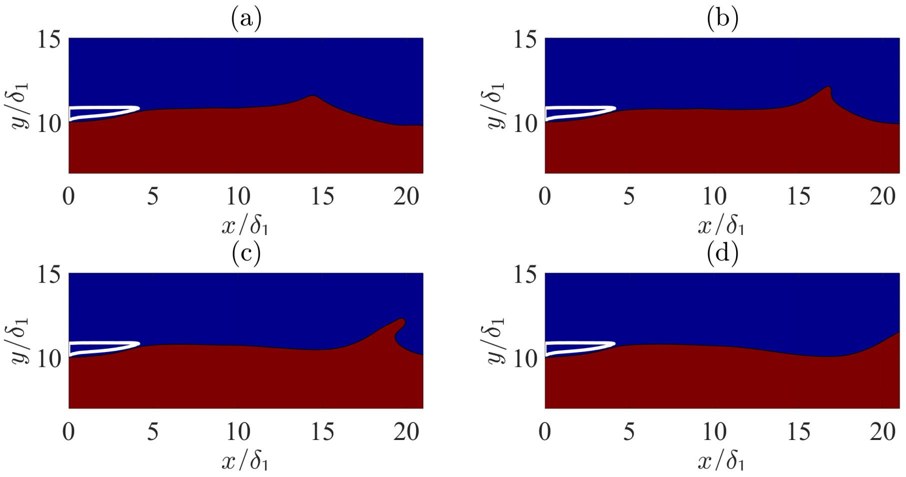

Figure 2: Interface location (black curve) and volume fraction field C ($C = 1$ depicted in red, $C = 0$ in blue) at different time instants: $t/t_{ref} = 70$ (a); 80 (b); 90 (c); 100 (d). The white curve in all panels denotes the wake region extension, while the black curve highlights the instantaneous location of the interface.

A summarizing overview of the physical quantities and the main corresponding dimensionless parameters involved in the problem is reported in Tables 1 and 2. Note that the only parameter varied in the analysis is the splitter plate thickness e, to span both regimes where $e/\delta_1 < 1$ and $e/\delta_1 > 1$ identified by previous literature works [16, 25]. Moreover, as is common for the simulation of two-phase mixing layers in the fast/slow fluid streams numerical setup [16, 9], gravitational acceleration g is neglected. For such a configuration, the Froude number is indeed on the order of $Fr = U_1^2/(g\delta_1) = \mathcal{O}(10^4)$, indicating that the inertial forces from the fast shearing phase dominate over gravitational effects. Note also that a value of $r_\rho = 0.1$ is employed for the density ratio to balance the computational feasibility with the physical accuracy of the numerical investigation. Indeed, while a lower r_ρ value would more closely approximate air-water configurations, the numerical stiffness introduced at low density ratios significantly slows down the solution to the pressure Poisson problem arising in the numerical discretization of the Navier-Stokes equations (see following Section 3.1).

A typical sequence of the appearance and propagation of the interfacial wave is depicted in Fig. 2, corresponding to the parameters reported in Table 2 with $e/\delta_1 = 1$. Note that values of the Reynolds number $Re = 1000$ and dynamic pressure ratio $M = 10$ lie in the so-called global G-regime identified by Fuster *et al.* [16], and that $t_{ref} = \delta_1/U_1$ has been considered as reference time. By inspection of Fig. 2, it can be seen that the wave appears periodically within the simulation domain and moves downstream, increasing in size as its top goes beyond the fast stream boundary layer (Fuster et al. [16]). Once the wave becomes sufficiently large, it generates suction and alters the interface height upstream. As it continues to travel downstream, the liquid level gradually returns to its original state, and a new wave forms.

3 Methodology

3.1 Numerical simulation

The two-phase mixing layer flow originating downstream of the splitter plate is modelled with the one-fluid formulation of incompressible Navier-Stokes equations [26]. In Einstein notation, the system reads as

$$\frac{\partial u_i}{\partial x_i} = 0, \tag{5a}$$

$$\rho\left(\frac{\partial u_i}{\partial t} + u_j\frac{\partial u_i}{\partial x_j}\right) = -\frac{\partial p}{\partial x_i} + \frac{\partial}{\partial x_j}\left[\mu\left(\frac{\partial u_i}{\partial x_j} + \frac{\partial u_j}{\partial x_i}\right)\right] + F_\gamma, \tag{5b}$$

$$\frac{\partial C}{\partial t} + \frac{\partial C u_i}{\partial x_i} = 0. \tag{5c}$$

The vector $\mathbf{u} = (u, v)$ represents the flow velocity, while p is the pressure. The force per unit volume due to the surface tension is denoted as $F_\gamma = \gamma\kappa n_i \delta_S$, where γ is the surface tension coefficient, κ the mean interface curvature, and $\mathbf{n}$ the outward pointing normal vector to the interface. The Dirac distribution function δ_S is equal to 1 at the interface, and 0 elsewhere. The density ρ and viscosity μ fields are discontinuous across the interface separating the two fluids, namely

$$\rho = \rho_1 + (\rho_2 - \rho_1)C, \tag{6a}$$

$$\mu = \mu_1 + (\mu_2 - \mu_1)C, \tag{6b}$$

where subscripts 1 and 2 refer to the upper (faster) and lower (slower) phases, and the volume fraction field C is equal to either 0 or 1 in the two regions, respectively.

The system (5a)-(5c) is solved using the finite volume method implemented in the open-source code BASILISK, an improved version of Gerris [27] that has been extensively used and validated to investigate the dynamics of two-phase mixing layer flows (among others, see [16, 28, 29]). The code employs the volume-of-fluid (VOF) method [26, 30, 31] to track the interface on a quadtree-structured grid, allowing in general for adaptive mesh refinement based on a criterion of wavelet-estimated discretization error [32]. In this work, a uniform mesh with constant grid spacing has been employed for all simulations. The calculation of the surface tension term is based on the balanced continuum surface force technique [33], which is coupled with a height-function curvature estimation to avoid the generation of spurious currents. For exhaustive details about the code, the reader is referred to Popinet [27, 34] and to the official software website (`http://basilisk.fr`).

We explicitly highlight here that numerical methods for two-phase flow problems constitute a vast body of literature, and that strategies different from the VOF approach adopted in this work could be more effective for different flow configurations. Among the most widely adopted interface-resolving approaches are the Level Set (LS) [35, 36], Front Tracking [37, 38], and Phase Field methods [39, 40]. The LS method represents the fluid interface as a signed distance function, offering accurate curvature calculations and smooth evolution, but it requires frequent reinitialization and may lead to mass loss. Front Tracking methods explicitly track the interface with marker points or separate meshes, providing sharp resolution and accurate surface tension modelling, but at the cost of complex mesh handling. Phase Field methods, based on diffuse interface theory, model the interface as a continuous transition region. They are especially effective for handling topological changes (e.g., merging and breakup), though they introduce artificial interface thickness and require high spatial resolution. For dispersed-phase flows, such as dilute droplet or bubble suspensions, Lagrangian methods like Lagrangian Particle Tracking (LPT) [41, 42] and Smoothed Particle Hydrodynamics (SPH) [43] are commonly used. These techniques are computationally efficient and well-suited for dilute systems, but may become inaccurate at higher phase fractions due to unresolved interactions. In contrast, Euler–Euler models [44, 45] treat both phases as interpenetrating continua with averaged conservation equations and interfacial exchange terms. These models are particularly effective for high phase-fraction flows and are widely used in industrial and engineering applications. Finally, Lattice Boltzmann Methods (LBM) [46, 47] offer a mesoscopic alternative based on kinetic theory, with natural parallelism and flexible multiphase extensions.

3.2 Dynamic mode decomposition

To investigate the two-phase mixing layer global dynamics, we apply the dynamic mode decomposition (DMD) analysis [48] to the flow data obtained from volume-of-fluid numerical simulations. The DMD algorithm can be seen as a data-driven optimization problem, where one seeks the best fit linear matrix operator **A** approximating the time evolution of the dynamical system of interest [49, 50, 51].

Given a sequence of snapshots $\mathbf{x}_k$ representing the state of the system at discrete time intervals, the dynamics can be (linearly) approximated as

$$\mathbf{x}_{k+1} = \mathbf{A}\ \mathbf{x}_k, \tag{7}$$

where $t_{k+1} = t_k + \Delta t$, and the time spacing Δt is assumed small enough to accurately resolve the dynamics. The matrix is approximated from a collection of snapshot pairs [52] of the system dynamics, $\{(\mathbf{x}(t_k), \mathbf{x}(t'_k))\}_{k=1}^{m}$, where $t'_k = t_k + \Delta t$. Each of the $m_t = m + 1$ snapshots typically represents the measurement of the system state, such as the density and/or velocity field in all the $n = N_x \times N_y$ points of the computational domain, reshaped in a column vector.

Rearranging the flow snapshots in the two data matrices **X** and **X'**,

$$\begin{aligned} \mathbf{X} &= \begin{bmatrix} | & | & & | \\ \mathbf{x}(t_1) & \mathbf{x}(t_2) & \cdots & \mathbf{x}(t_m) \\ | & | & & | \end{bmatrix}, \\ \mathbf{X}' &= \begin{bmatrix} | & | & & | \\ \mathbf{x}(t'_1) & \mathbf{x}(t'_2) & \cdots & \mathbf{x}(t'_m) \\ | & | & & | \end{bmatrix}, \end{aligned} \tag{8}$$

one can rewrite Eq. (7) as

$$\mathbf{X}' = \mathbf{A}\mathbf{X}, \tag{9}$$

where the best-fit matrix **A** establishes a linear relationship that advances the snapshot measurements forward in time. Such a matrix can be seen as the result of an optimization problem,

$$\mathbf{A} = \min_{\mathbf{A}} \left\| \mathbf{X}' - \mathbf{A}\mathbf{X} \right\|_F = \mathbf{X}'\mathbf{X}^{+}, \tag{10}$$

where $\|\|_F$ denotes the Frobenius norm and the $\mathbf{X}^+$ is the pseudoinverse of the matrix $\mathbf{X}$, which is computed via Singular Value Decomposition (SVD) of $\mathbf{X} = \mathbf{U}\boldsymbol{\Sigma}\mathbf{V}^*$ [53], namely as

$$\mathbf{X}^+ = \mathbf{V}\boldsymbol{\Sigma}^{-1}\mathbf{U}^*, \tag{11}$$

where $\mathbf{U}^*$ is the conjugate and transpose of the proper orthogonal decomposition eigenmodes matrix $\mathbf{U}$, and $\boldsymbol{\Sigma}$ is the diagonal matrix containing the singular values.

Since the matrix $\mathbf{A}$ has n^2 elements, its eigendecomposition is practically unfeasible when dealing with highly resolved flow snapshots. Observing that the matrices $\mathbf{X}$ and $\mathbf{X}'$ typically have far more rows than columns, $m << n$, it is clear that $\mathbf{A}$ has at most m non-zero eigenvalues and non-trivial eigenvectors. Therefore, it is possible to project $\mathbf{A}$ onto the first r POD modes $\mathbf{U}_r$, and approximate the pseudoinverse using the rank-r SVD approximation of $\mathbf{X}$,

$$\tilde{\mathbf{A}} = \mathbf{U}_r^*\mathbf{A}\mathbf{U}_r = \mathbf{U}_r^*\mathbf{X}'\mathbf{X}^+\mathbf{U}_r = \mathbf{U}_r^*\mathbf{X}'\mathbf{V}_r\boldsymbol{\Sigma}_r^{-1}\mathbf{U}_r^*\mathbf{U}_r = \mathbf{U}_r^*\mathbf{X}'\mathbf{V}_r\boldsymbol{\Sigma}_r^{-1}. \tag{12}$$

It is thus possible to approximate the spectral decomposition of $\mathbf{A}$ with $\tilde{\mathbf{A}}$,

$$\tilde{\mathbf{A}}\mathbf{W} = \mathbf{W}\mathbf{L}, \tag{13}$$

where the diagonal matrix $\boldsymbol{L}$ contains the DMD eigenvalues, and the columns of $\mathbf{W}$ store the eigenvectors. As a consequence, the eigenvectors of $\mathbf{A}$ are constructed as

$$\boldsymbol{\Phi} = \mathbf{X}'\mathbf{V}_r\boldsymbol{\Sigma}_r{}^{-1}\mathbf{W}, \tag{14}$$

and they represent the so-called DMD modes of the flow system [54].

Once the DMD modes ϕ_j and eigenvalues l_j $(j = 1, \ldots, r)$ have been obtained, one can approximate the state of the system with the following spectral expansion,

$$\hat{\mathbf{x}}_k = \sum_{j=1}^{r} \boldsymbol{\phi}_j l_j^{k-1} b_j = \boldsymbol{\Phi}\mathbf{L}^{k-1}\mathbf{b}, \tag{15}$$

where b_j are the mode amplitudes depending on the initial condition,

$$\mathbf{b} = \boldsymbol{\Phi}^+\mathbf{x}_1, \tag{16}$$

and $\mathbf{\Phi}^+$ is the pseudoinverse of $\mathbf{\Phi}$. The continuous-time equivalent of Eq. (15) is finally obtained by introducing the continuous eigenvalues $\omega_j = \log(l_j)/\Delta t$,

$$\hat{\mathbf{x}}(t) = \sum_{j=1}^{r} \boldsymbol{\phi}_j e^{\omega_j t} b_j = \mathbf{\Phi} \exp(\mathbf{\Omega} t)\mathbf{b}. \tag{17}$$

4 Results

The two-phase mixing layer global dynamics by variation of the plate-to-vorticity thickness ratio e/δ_1 are investigated in this section, which shows results of the two-dimensional volume-of-fluid simulations and dynamic mode decomposition algorithm. The analysis begins with a study of the time-averaged velocity fields, providing insights into the spatial structure of the two-phase mixing layer (Section 4.1). The unsteady dynamics are then investigated employing a local analysis (i.e., at selected locations within the flow field) in Section 4.2, in alignment with methodologies commonly employed in the existing literature. The last two Sections 4.3 and 4.4 represent the core contributions of the work. Section 4.3 shows results of the data-driven global stability analysis performed through the dynamic mode decomposition, focusing attention on the identification of flow structures and associated dominant oscillation frequencies. In Section 4.4, a physical interpretation of the frequency shift characterizing the mixing layer global dynamics as e/δ_1 increases is provided. In particular, an explanation linking this phenomenon to the near-field dynamics induced by the splitter plate geometry is formulated, and it is finally corroborated by the application of a simple control strategy at the plate edge.

4.1 Mean flow analysis

The time-averaged (mean) streamwise velocity contour u/U_1 in the near-field region of the two-phase mixing layer flow is shown in Fig. 3 by variation of e/δ_1, which ranges from 0.5 (panel (a)) to 1.5 (panel (c)). Note that all physical quantities have been normalized by using characteristic spatial and velocity scales of the phenomenon, namely the vorticity thickness δ_1 and the velocity U_1. Moreover, although the numerical simulations are run for a total time of $t_f = 2000 \cdot t_{ref}$, only the last 1000 reference times are considered in the computation of the mean flow, as well as in the temporal analysis provided

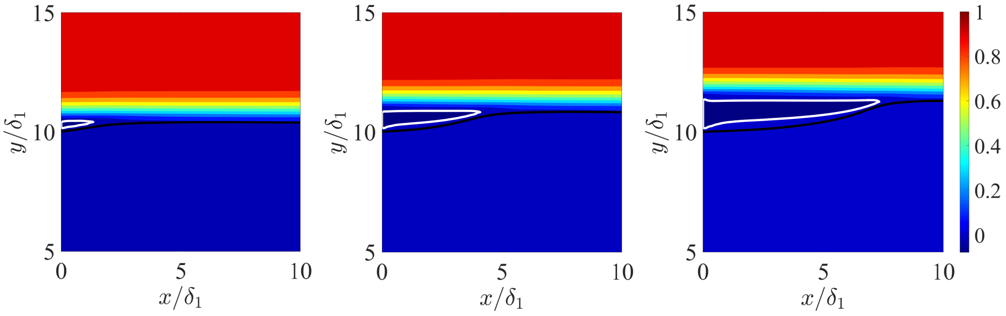

(a) (b) (c)

Figure 3: Time-averaged streamwise velocity contour u/U_1 by variation of the plate-to-vorticity thickness ratio: $e/\delta_1 = 0.5$ (a); $e/\delta_1 = 1.0$ (b); $e/\delta_1 = 1.5$ (c). The white curve in all panels denotes the wake region extension, while the black curve highlights the time-averaged location of the interface.

later on in this Section. In this way, the initial transient phase is discarded, ensuring that results reflect fully developed and stationary flow conditions.

After issuing from the inlet section ($x = 0$), the two fluid streams meet downstream of the splitter plate. By moving along the streamwise x direction, two distinct regions can be detected for all cases: a wake ($0 < x < x_w$) and a pure mixing layer ($x > x_w$) region. The wake length x_w has been calculated as the last streamwise station (starting from $x = 0$) where $u < 0$, i.e., $u > 0$ for $x > x_w$. The fast and slow phases are separated by the time-averaged interface, denoted as a black curve in all panels of Fig. 3. It can be seen that, as e/δ_1 progressively increases, the wake recirculation region elongates. This effect is further quantified in Fig. 4, which illustrates the velocity profiles along the normal-to-flow direction $u(y)$ by variation of e/δ_1 at selected streamwise locations within the flow field, ranging from $x/\delta_1 = 2$ (panel (a)) to $x/\delta_1 = 12$ (panel (d)).

The velocity profiles in Fig. 4 exhibit a transition from the free-stream values U_1 ($y/\delta_1 > 13$) and U_2 ($y/\delta_1 < 9$) to the interfacial values ($9 < y/\delta_1 < 13$), where the strongest spatial variations occur. Moreover, it can be seen that the velocity deficit induced by the plate in the near-field region augments as e/δ_1 increases (see red, black, and blue curves in Fig. 4(a)-(b)). On the other hand, the progressive momentum exchange between the fast and the slow fluid streams leads to the absorption of the velocity deficit as the streamwise direction is increased (Fig. 4(c)-(d)). A final overview of the

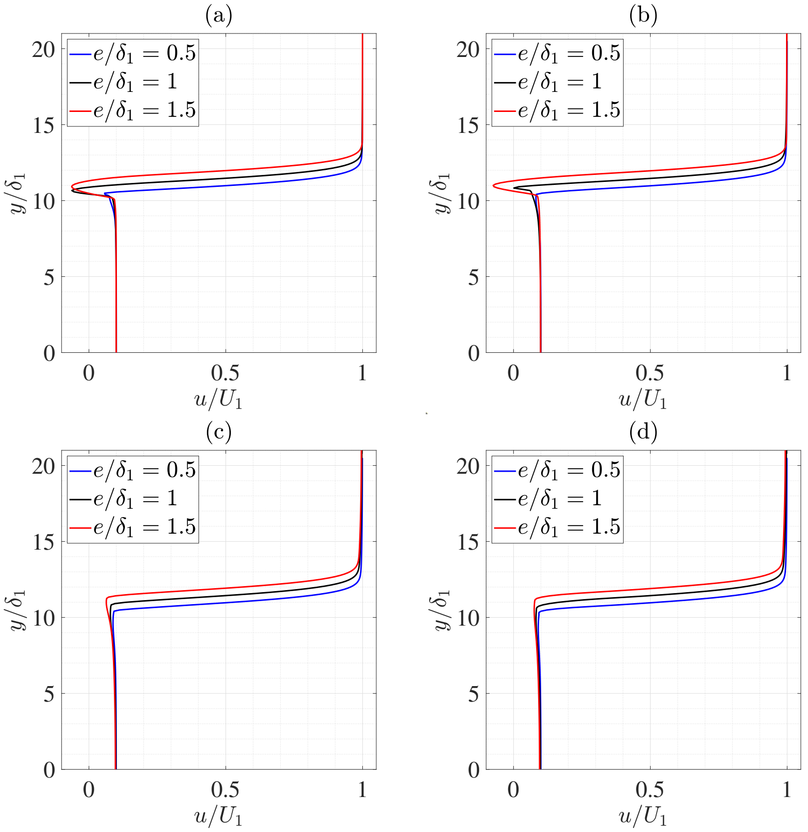

Figure 4: Velocity profiles along the normal-to-flow direction $u(y)/U_1$ by variation of e/δ_1 at different streamwise x locations: (a) $x/\delta_1 = 2$; (b) $x/\delta_1 = 4$; (c) $x/\delta_1 = 8$; (d) $x/\delta_1 = 12$.

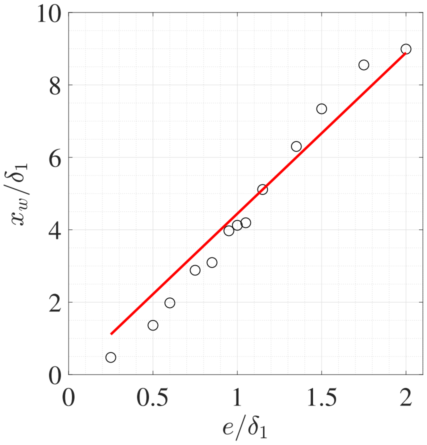

Figure 5: Wake region extension x_w/δ_1 as a function of the plate-to-vorticity thickness ratio e/δ_1. The red curve represents the least-squares linear regression of the numerical data (black circles).

wake region extension as a function of e/δ_1 is shown in Fig. 5, where more plate-to-vorticity thickness values are provided in the range $e/\delta_1 \in [0.25, 2]$. The numerical data (black circles) highlight an almost linear increase (red curve) of the wake length x_w with the plate thickness e. This trend can be interpreted through a compelling analogy with the canonical (one-phase) backward-facing step (BFS) laminar flow, by considering the slower, denser stream as effectively acting like a rigid boundary for the faster, lighter stream flowing above it. The analogy, of course, holds only in the proximity of the splitter plate edge, where the wake region develops and the wavy interface deformation has not occurred yet. In the BFS configuration [55], a fluid with velocity U_1 and density ρ_1 flows through a channel of height H_1, then encounters a sudden expansion due to a step of height e, which induces flow separation and subsequent reattachment downstream at a distance x_w from the step. In such flows, the non-dimensional reattachment length x_w/e depends primarily on the Reynolds number based on the channel height, $Re_H = \rho_1 U_1 H_1/\mu$. Since all the cases considered in Fig. 5 share the same Re_H but differ in e, the ratio x_w/e remains approximately constant, which explains the linear relationship observed between x_w and e.

4.2 Local temporal dynamics

The unsteady dynamics of the two-phase mixing layer flow are first analyzed from a local perspective, namely by computing the Power Spectral Density (PSD) of the interface oscillations at distinct streamwise locations within the flow field. Results are shown in Fig. 6, where the time evolution of the interface elevation $y_{int}(x,t)$ (left panels) and the corresponding frequency spectra (right panels) are shown for $e/\delta_1 = 0.5$ (panels (a)-(b)), $e/\delta_1 = 1.0$ (panels (c)-(d)) and $e/\delta_1 = 1.5$ (panels (e)-(f)) at the locations $x/\delta_1 = 8$ (blue curves), 10 (black curves) and 14 (red curves).

For $e/\delta_1 = 0.5$, the interaction between the fast and slow fluid streams results in a Kelvin–Helmholtz instability, which determines the wavy dynamics of the interface characterized by the temporal (reduced) frequency $St_{ML} = f\delta_1/U_1 \approx 0.018$. This is evident from the time signals and corresponding frequency spectra reported in Fig. 6(a)-(b), which display a peak at St_{ML} for all the streamwise stations considered (see blue, black and red curves in Fig. 6(b)). Note that the order of magnitude of the dominant frequency $St_{ML} = \mathcal{O}(10^{-2})$ strictly matches the numerical predictions made by Fuster *et al.* [16] through VOF simulations and local linear stability analysis.

For $e/\delta_1 = 1.0$, the dominant frequency of the interface oscillation shifts to the lower value $St^W_{ML} \approx 0.012$ (see Fig. 6(c)-(d)), which is maintained by further increasing the plate-to-thickness ratio up to $e/\delta_1 = 1.5$ (see Fig. 6(e)-(f)). This result is in agreement with previous experimental and numerical findings by Ben Rayana *et al.* [25] and Fuster *et al.* [16], which were obtained for air-water conditions. By means of the local analysis, these authors found a shift of the flow dominant oscillation frequency beyond a critical threshold $e/\delta_1 = \mathcal{O}(1)$, opening up a question regarding the driving mechanisms underlying this phenomenon. We investigate this problem in the following Sections 4.3 and 4.4 by applying dynamic mode decomposition to the numerical data described so far, to identify the global spatio-temporal flow structures associated with the dominant frequencies and the physical mechanisms responsible for the frequency shift.

4.3 Global spatio-temporal dynamics

The global dynamics of the two–phase mixing layer are here analyzed by applying dynamic mode decomposition to the flow snapshots computed by 2D-VOF simulations. In particular, m_t=100 instances of the density field $\rho =$

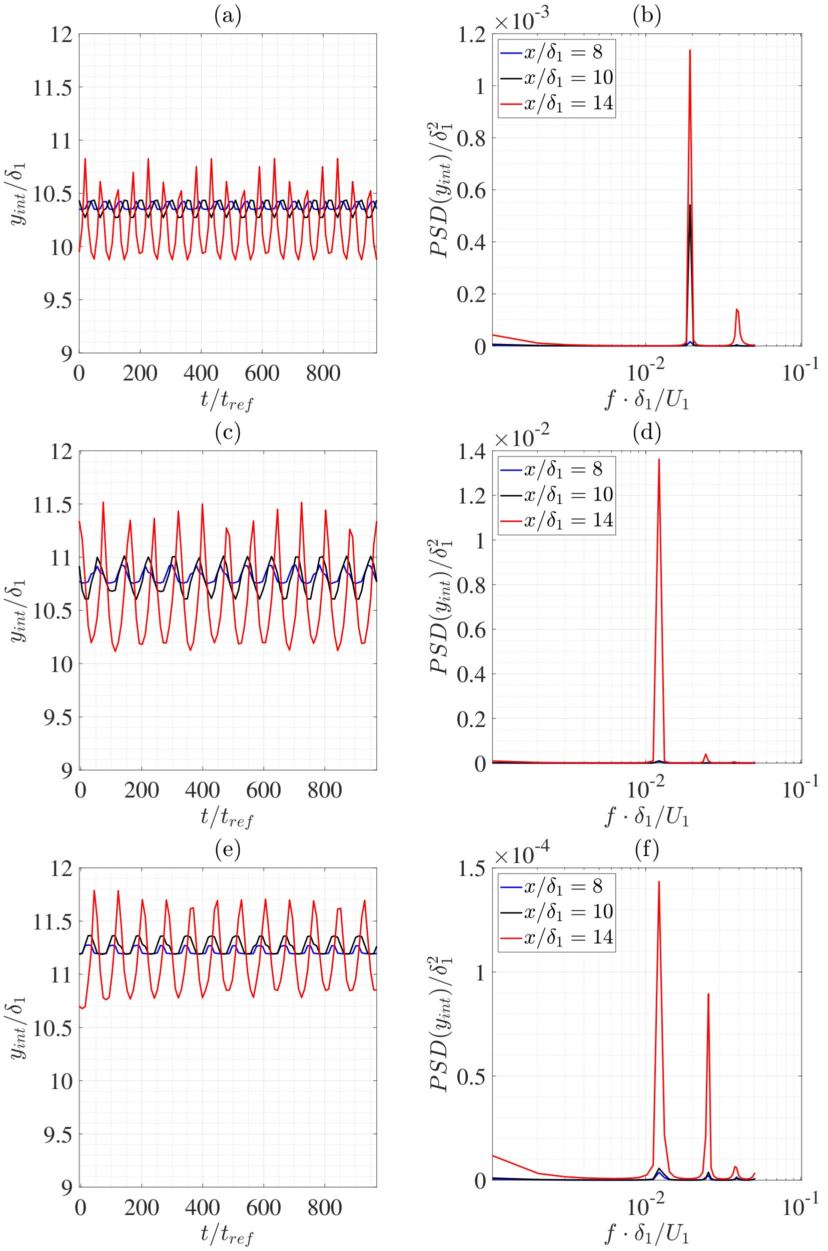

Figure 6: Time evolution of the interface elevation y_{int}/δ_1 (left columns) and corresponding power spectral density (right columns) at different streamwise locations x/δ_1 by variation of the plate-to-vorticity thickness ratio: $e/\delta_1 = 0.5$ ((a)-(b)); $e/\delta_1 = 1.0$ ((c)-(d)); $e/\delta_1 = 1.5$ ((e)-(f)).

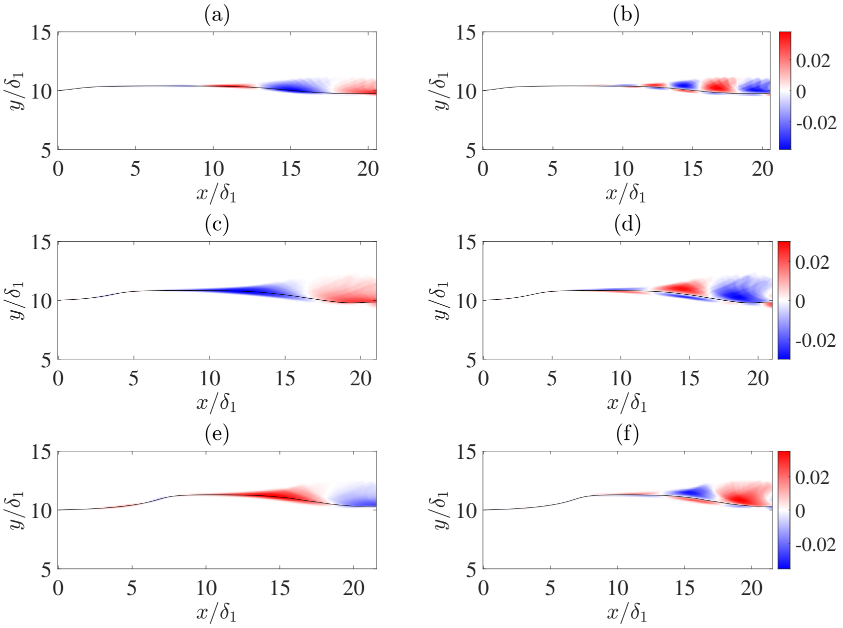

Figure 7: First (left panels) and second (right panels) dynamic mode decomposition leading modes (i.e. with the largest growth rate) by variation of the plate-to-thickness ratio: $e/\delta_1 = 0.5$ ((a)-(b)); $e/\delta_1 = 1.0$ ((c)-(d)); $e/\delta_1 = 1.5$ ((e)-(f)).

$\rho_1 + (\rho_2 - \rho_1) \cdot C$ are selected with a time-spacing equal to $\Delta t = 10 \cdot t_{ref}$, where $C(x, y)$ is the two-dimensional volume fraction field. The flow snapshots are collected into the matrices $\mathbf{X}'$ and $\mathbf{X}$ (see Eq. (8) in Section 3.2) and the DMD algorithm is applied to compute the global eigenmodes and eigenvalues of the flow by variation of the plate-to-vorticity thickness parameter e/δ_1.

Results of the analysis are first reported in Figs. 7-8, which show the two leading DMD eigenmodes ϕ_1 and ϕ_2 (i.e. with the largest growth rates σ_1^R and σ_2^R) and the spectrum of the first $r = 11$ eigenvalues $\sigma_k = \sigma_k^R + j\sigma_k^I$ ($k = 0, \ldots, r$) for $e/\delta_1 = 0.5$ (panels (a)-(b)), $e/\delta_1 = 1.0$ (panels (c)-(d)) and $e/\delta_1 = 1.5$ (panels (e)-(f)), respectively. Note that the eigenvalues ω (see Eq. (17) in Section 3.2) have been scaled as $\sigma = \omega/(2\pi)$, to obtain the temporal frequencies. For all cases, it can be seen that the leading modes correspond to coherent spatio-temporal waves travelling at the interface between the two fluids (see Fig. 7). Since the growth rate of these modes is practically zero (see Fig. 8), meaning they neither grow nor decay over time, they are linked to the propagation of the Dimotakis wave, which determines the oscillatory dynamics of the interface.

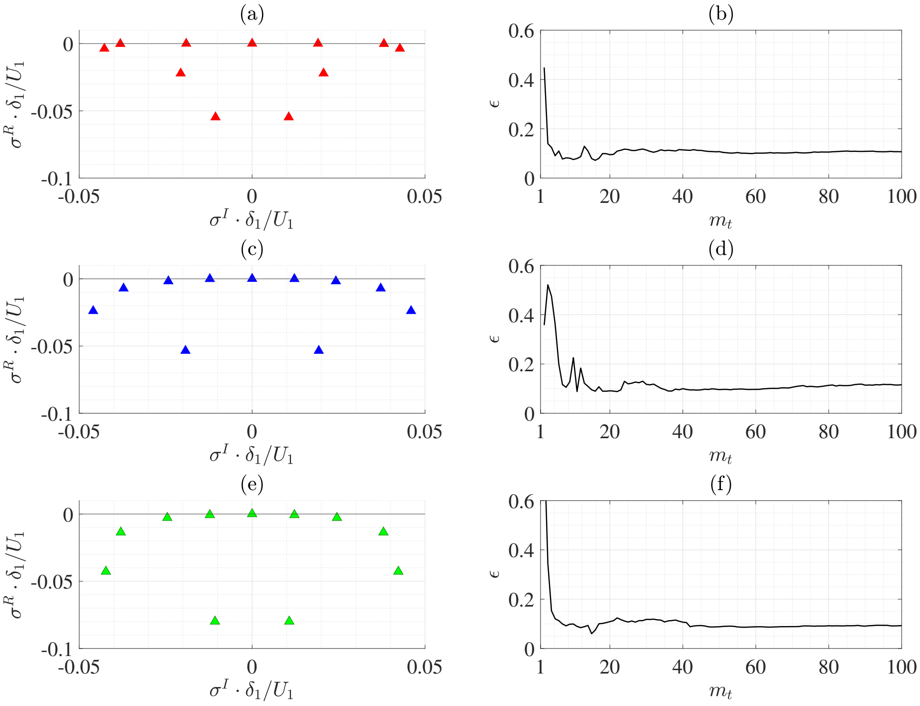

Figure 8: Global eigenvalues spectra of the two-phase mixing layer flow dynamics obtained by dynamic mode decomposition (left panels) and corresponding reconstruction error norm (right panels) by variation of the plate-to-thickness ratio: $e/\delta_1 = 0.5$ ((a)-(b)); $e/\delta_1 = 1.0$ ((c)-(d)); $e/\delta_1 = 1.5$ ((e)-(f)).

The temporal frequency associated with the leading eigenmode ϕ_1 (left panels in Fig. 7) strictly matches predictions of the local analysis, namely it shifts from $\sigma_1^I \delta_1/U_1 \approx 0.018$ for $e/\delta_1 = 0.5$ (see Fig. 8(a)) to $\sigma_1^I \delta_1/U_1 \approx 0.012$ for $e/\delta_1 = 1.0$ (Fig. 8(c)) and $e/\delta_1 = 1.5$ (Fig. 8(e)). Correspondingly, the spatial wavelength of the mode increases from $\lambda_1/\delta_1 \approx 2.7$ (Fig. 7(a)) to $\lambda_1/\delta_1 \approx 4$ (Fig. 7(c) and (e)) as the plate-to-vorticity thickness increases, such as to maintain the travelling velocity (scaling as the product between frequency and wavelength) constant. Note that the zero-frequency eigenvalue σ_0 shown in panels (a), (c), and (e) of Fig. 8 corresponds to the mean (i.e., time-averaged) density flow field. Moreover, panels (b), (d), and (f) of Fig. 8

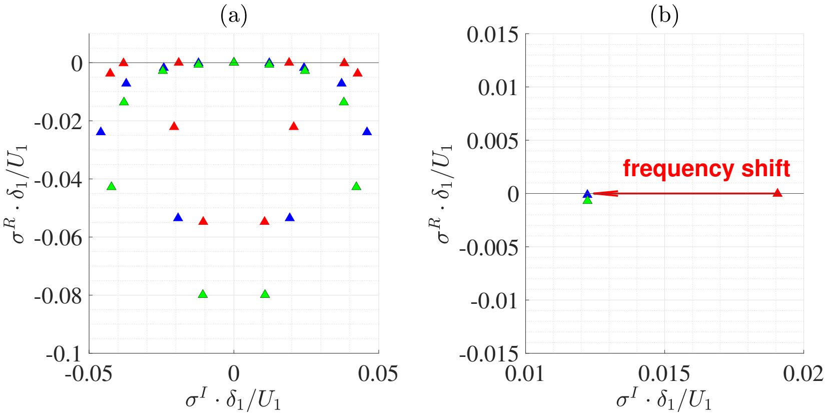

Figure 9: DMD spectra by variation of the plate-to-thickness ratio e/δ_1 (a) with zoom on the frequency shift (b): $e/\delta_1 = 0.5$ (red markers); $e/\delta_1 = 1.0$ (blue markers); $e/\delta_1 = 1.5$ (green markers).

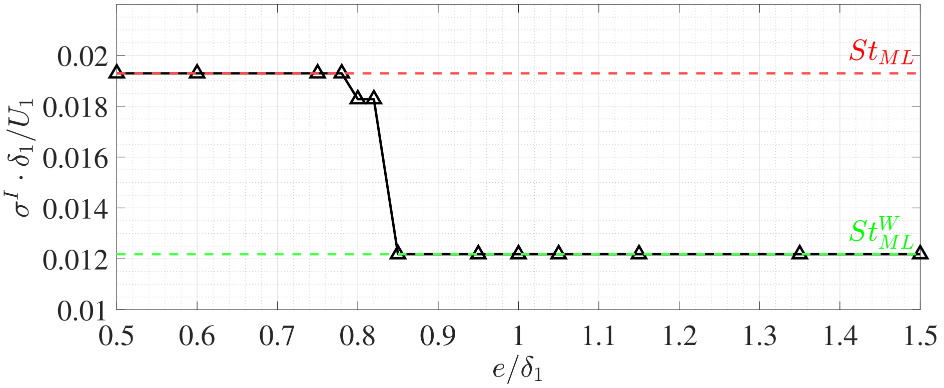

Figure 10: Global frequency of the leading DMD mode as a function of the plate-to-thickness ratio e/δ_1, highlighting the frequency shift from St_{ML} (red dashed line) to St_{ML}^W (green dashed line) occurring at $e/\delta_1 \approx 1$.

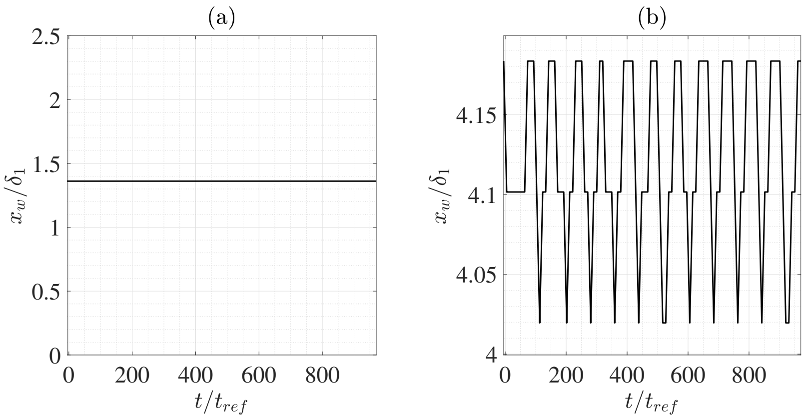

Figure 11: Temporal evolution of the wake tip location x_w for (a) $e/\delta_1 = 0.5$ and (b) $e/\delta_1 = 1.0$.

demonstrate the convergence of the eigenvalue spectra computed for $e/\delta_1 =$ 0.5, 1.0, and 1.5, respectively. It can be appreciated that the maximum reconstruction error $\epsilon = ||\boldsymbol{\rho} - \tilde{\boldsymbol{\rho}}||_2/||\boldsymbol{\rho}||_2$ between the ground-truth VOF solution $\boldsymbol{\rho}$ and the DMD approximation $\tilde{\boldsymbol{\rho}}$ (see Eq. (17) in Section 3.2) reaches a plateaux for $m_t > 80$ in all cases.

The change of the flow dominant global frequency as the plate-to-vorticity thickness increases is enhanced in Fig. 9, where the DMD eigenspectra corresponding to $e/\delta_1 = 0.5$ (red markers), 1.0 (blue) and 1.5 (green) are superposed to each other, and in Fig. 10, which reports the dominant eigenfrequency $\sigma_1^I \delta_1/U_1$ for more values of the plate-to-vorticity thickness ratio in the range $e/\delta_1 \in [0.5, 1.5]$. The frequency-shift from $St_{ML} \approx 0.018$ to $St_{ML}^W \approx 0.012$ occurring at $e/\delta_1 \approx 1$ can be clearly appreciated. In the following Section 4.4, we shed light on the physical mechanisms driving this phenomenon.

4.4 The intermodulation mechanism

To investigate the driving mechanisms responsible for the frequency shift highlighted in previous Sections 4.2-4.3, we start by inspection of the 2D-VOF unsteady flow field. In particular, we monitor the position of the wake tip x_w as a function of time t in the numerical simulations performed by variation of the plate-to-vorticity thickness ratio. Results are reported in Fig. 11 for $e/\delta_1 = 0.5$ (panel (a)) and $e/\delta_1 = 1.5$ (panel (b)), respectively.

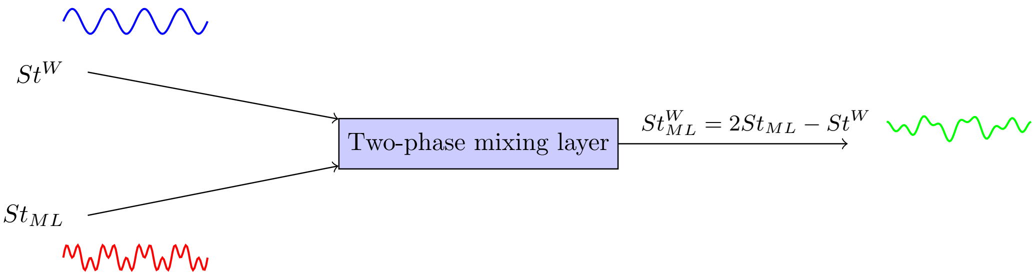

Figure 12: Schematic representation of the intermodulation mechanism. The nonlinear interaction between the wake St^W and mixing layer St_{ML} characteristic frequencies determines the shift to St^W_{ML}.

Interestingly, it can be observed that the wake region undergoes a transition from steady conditions to a periodic regime as e/δ_1 increases, with the frequency of the wake oscillations being equal to $St^W \approx 0.024$ in the latter case.

It is therefore argued that the observed frequency shift in the mixing layer global dynamics is determined by the interaction between the wake ($St^W \approx 0.024$) and the mixing layer ($St_{ML} \approx 0.018$) characteristic frequencies, resulting in the third-order intermodulation frequency $St^W_{ML} = 2St_{ML} - St^W \approx 0.012$.

The intermodulation mechanism is a well-known phenomenon occurring in electronics (and more generally in signal processing) where signals containing two or more different frequencies undergo amplitude modulation, due to nonlinearities or time-varying properties of the system in which they propagate [56]. Unlike harmonic distortion, which produces additional frequencies as integer multiples (harmonics) of the original ones, intermodulation generates new terms at the sum and difference of the original frequencies, as well as at sums and differences of multiples of those frequencies. In the present case, the nonlinear interaction between the signal St^W, due to the wake transition from steady to periodic regime, and the mixing layer natural frequency St_{ML}, related to the travelling wave propagating at the fluids interface, determines the third-order intermodulation product St^W_{ML} observed as e/δ_1 increases. A schematic representation of the intermodulation mechanism is reported in Fig. 12.

To further illustrate the emergence of such a mechanism, let us introduce a simple toy model. Consider an input signal composed of two sinusoidal components:

$$x(t) = a_1 \cos(2\pi f_1 t) + a_2 \cos(2\pi f_2 t), \tag{18}$$

where f_1 and f_2 represent two distinct frequencies, and a_1, a_2 their respective amplitudes. Let the system response be governed by a weakly nonlinear input–output relationship, retaining terms up to third order:

$$y(t) = b_1 x(t) + b_2 x^2(t) + b_3 x^3(t), \tag{19}$$

where b_1, b_2, b_3 are system-dependent constants. Intermodulation effects arise from the nonlinear terms. For the purpose of our analysis, we focus on the cubic component, which is responsible for third-order intermodulation products. Substituting Eq. (18) into Eq. (19) and expanding the cubic term gives:

$$\begin{aligned} x^3(t) = a_1^3 \cos^3(2\pi f_1 t) &+ 3a_1^2 a_2 \cos^2(2\pi f_1 t)\cos(2\pi f_2 t) \\ &+ 3a_1 a_2^2 \cos(2\pi f_1 t)\cos^2(2\pi f_2 t) + a_2^3 \cos^3(2\pi f_2 t), \end{aligned} \tag{20}$$

where each term contributes to harmonic and intermodulation content. We now focus on the third term on the right-hand side of Eq. (20) and use the trigonometric identity $\cos^2(\theta) = \frac{1}{2} + \frac{1}{2}\cos(2\theta)$, yielding:

$$\begin{aligned} 3a_1 a_2^2 \cos(2\pi f_1 t)\cos^2(2\pi f_2 t) &= 3a_1 a_2^2 \cos(2\pi f_1 t)\left(\frac{1}{2} + \frac{1}{2}\cos(4\pi f_2 t)\right) \\ &= \frac{3}{2} a_1 a_2^2 \cos(2\pi f_1 t) + \frac{3}{2} a_1 a_2^2 \cos(2\pi f_1 t)\cos(4\pi f_2 t). \end{aligned} \tag{21}$$

We then apply the identity $\cos\theta_1 \cos\theta_2 = \frac{1}{2}[\cos(\theta_1 + \theta_2) + \cos(\theta_1 - \theta_2)]$ to rearrange the second term at the right-hand-side of Eq. (21), thus obtaining:

$$\frac{3}{2} a_1 a_2^2 \cos(2\pi f_1 t)\cos(4\pi f_2 t) = \frac{3}{4} a_1 a_2^2 \left[\cos\left(2\pi(f_1 + 2f_2)t\right) + \cos\left(2\pi(2f_2 - f_1)t\right)\right]. \tag{22}$$

The term $\cos\left(2\pi(2f_2 - f_1)t\right)$ represents a third-order intermodulation component arising in the nonlinear toy system (19) at the frequency $2f_2 - f_1$, consistent with the findings of this study. However, it is important to stress that, while such a toy model provides a valuable conceptual framework for illustrating how intermodulation components can originate from cubic nonlinearities, it remains an abstract representation. The actual physical mechanisms governing the generation and evolution of such components in the present two-phase flow system are still not fully understood and warrant further investigation. In particular, it is important to examine how nonlinear interactions between the dominant oscillatory modes—namely those associated with the frequencies St_W and St_{ML}—manifest within the full dynamics of the flow. An intriguing parallel emerges when considering the well-studied case of the wake flow behind an infinitely long circular cylinder [57], where the onset of nonlinear behavior—specifically, periodic vortex shedding via Hopf bifurcation—is linked to the effective presence of cubic nonlinearities hidden within the governing Navier–Stokes equations. In that case, the interaction between oscillatory modes and the base flow—when analyzed on slow timescales—was shown to give rise to a slow manifold, where the resulting dynamics could be approximated by cubic terms responsible for the bifurcation [58]. In the present context, the nonlinear phenomenon is different in nature—namely, the emergence of intermodulation components rather than a flow bifurcation—but, notably, it is captured by a simple mathematical model involving cubic nonlinearities. This analogy suggests that similar physical mechanisms may be at play in the two-phase mixing layer flow, potentially involving modal interactions and slow–fast dynamics akin to those observed in the cylinder problem. Uncovering and characterizing these mechanisms remains an open question that certainly requires further investigation in the future.

To corroborate that the intermodulation frequency St^W_{ML} arises from the interaction between St^W and St_{ML}, we performed an additional 2D-VOF simulation aiming at inhibiting the wake oscillations arising for $e/\delta_1 > 1$. In particular, we implemented a simple control strategy by superposing to the inflow boundary condition (see Eq. (1) in Section 2) the following actuation at the splitter plate edge,

$$u_c = U_c + A_c \sin(2\pi f_c + \phi_c), \quad H_2 < y \leq H_2 + e. \tag{23}$$

Among the various parameter combinations in Eq. (23) tested for designing the actuation, we found that the most effective configuration was $U_c = -0.01 \cdot U_1$ and $A_c = 0$, corresponding to a steady suction control with magnitude equal to 1% of the incoming fast stream velocity. As it can be appreciated in Fig. 13(a), the actuation is able to mitigate (although not to completely suppress) the wake oscillations characterizing the flow for $e/\delta_1 = 1.5$ (black

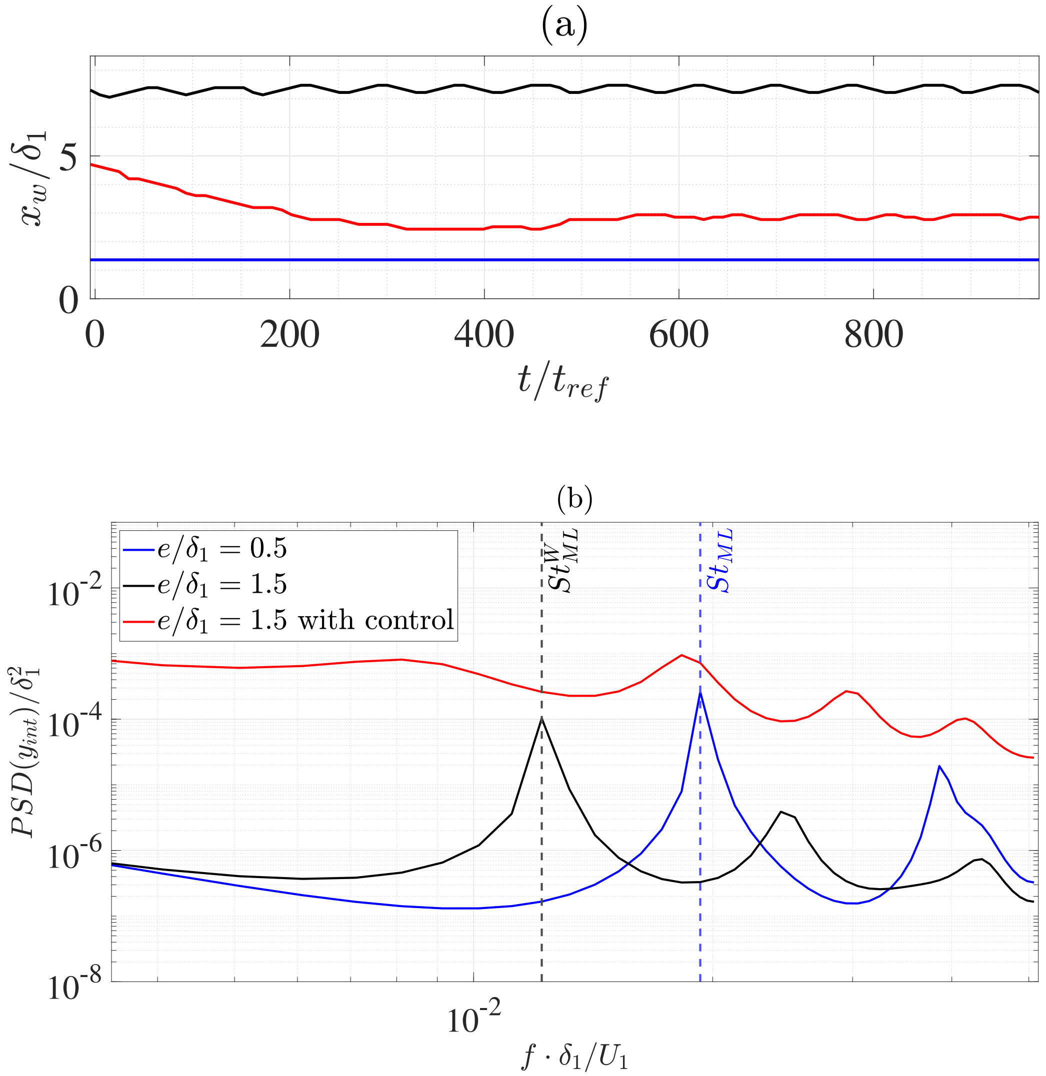

Figure 13: Temporal signals of the wake tip location (a) and power spectral density (PSD) of the interface oscillations at the streamwise station $x/\delta_1 = 10$ (b) for $e/\delta_1 = 0.5$ (blue curves) and $e/\delta_1 = 1.5$ before (black curves) and after (red curves) the control application (Eq. (23)) at the splitter plate edge. The vertical blue and black dashed lines in panel (b) denote the reduced frequencies St_{ML} and St^W_{ML}, respectively.

curve), thus making the controlled wake dynamics (red curve) closer to the $e/\delta_1 < 1$ regime (blue curve).

As a consequence of the wake mitigation, the dominant frequency of the two-phase mixing layer controlled dynamics exhibits a transition from St^W_{ML} towards the value St_{ML} for $e/\delta_1 = 1.5$, as it can be seen from the power spectral density signals reported in Fig. 13(b). We therefore conclude that the wake dynamics developing behind the splitter plate for $e/\delta_1 > 1$ serve as the primary mechanism driving the observed frequency shift. However, it is important to note that the simple control action employed here (Eq. (23)) does not fully suppress the wake oscillations. The application of more advanced control strategies, such as DMD-based control [59] or methods leveraging the concept of spectral submanifolds [60], is envisioned as a promising future development of this work.

5 Conclusions

The effect of the splitter plate thickness on the global dynamics of a planar two-phase mixing layer has been investigated through direct numerical simulation and dynamic mode decomposition analysis. The interfacial Kelvin-Helmholtz (KH) instability developing at the interface between the two fluids is crucially affected by the plate-to-vorticity thickness ratio e/δ_1. For $e/\delta_1 < 1$, the KH instability results in a wavy dynamics of the interface, whose temporal oscillations are characterized by the reduced frequency $St_{ML} = f\delta_1/U_1 \approx 0.018$. In such conditions, the DMD analysis has identified the dominant global mode of the flow as a spatio-temporal interfacial wave, which travels with the celebrated Dimotakis velocity and oscillates at the same frequency St_{ML}. On the other hand, for $e/\delta_1 > 1$, a sudden transition (shift) of the reduced frequency to the lower value $St^W_{ML} \approx 0.012$ has been observed. The leading spatio-temporal coherent structure identified by the DMD analysis correspondingly shifts to the same frequency. By inspection of the velocity field, it has been found that, as e/δ_1 increases, the wake region located right downstream of the splitter plate undergoes a transition from steady conditions to periodic oscillations at the reduced frequency $St^W \approx 0.024$. The observed frequency shift in the mixing layer global dynamics has been therefore ascribed to the interaction between the wake $\left(St^W\right)$ and the mixing layer (St_{ML}) characteristic frequencies, resulting in the third-order intermodulation frequency $St^W_{ML} = 2St_{ML} - St^W$. By applying a simple actuation at the splitter plate edge, it has been finally shown that inhibiting the wake oscillations restores the frequency St_{ML} even in the $e/\delta_1 > 1$ regime, thereby suppressing the frequency shift.

Acknowledgments

The numerical simulations included in the present work were performed on resources granted by CINECA under the ISCRA-C project ROMFLO-2.

Declaration of competing interest

The authors declare that they do not have any commercial or associative interest that represents a conflict of interest in connection with the work submitted.

Data availability

The data that support the findings of this study will be made available on reasonable request.

A Grid convergence analysis

The impact of mesh refinement on the numerical results presented in this study is evaluated through a grid convergence analysis. Results obtained using four different values of the maximum grid refinement level are compared: $N = 6, 7, 8$, and 9, where the total number of grid points in the computational domain is $2^N \times 2^N$. The four refinement levels correspond to minimum grid cell sizes of approximately $\Delta \approx \delta_1/3, \delta_1/6, \delta_1/12$, and $\delta_1/24$, respectively. The comparison is first shown in Fig. 14, which reports time-averaged profiles of the streamwise (panel (a)) and normal-to-flow (panel (b)) velocity components evaluated at $x/\delta_1 = 2$. This location is particularly sensitive to the mesh resolution, due to the high velocity gradient induced by the wake. It can be observed that the solution on the coarsest mesh ($N = 6$, blue curves) fails to accurately reproduce the velocity gradient, whereas the medium ($N = 7$,

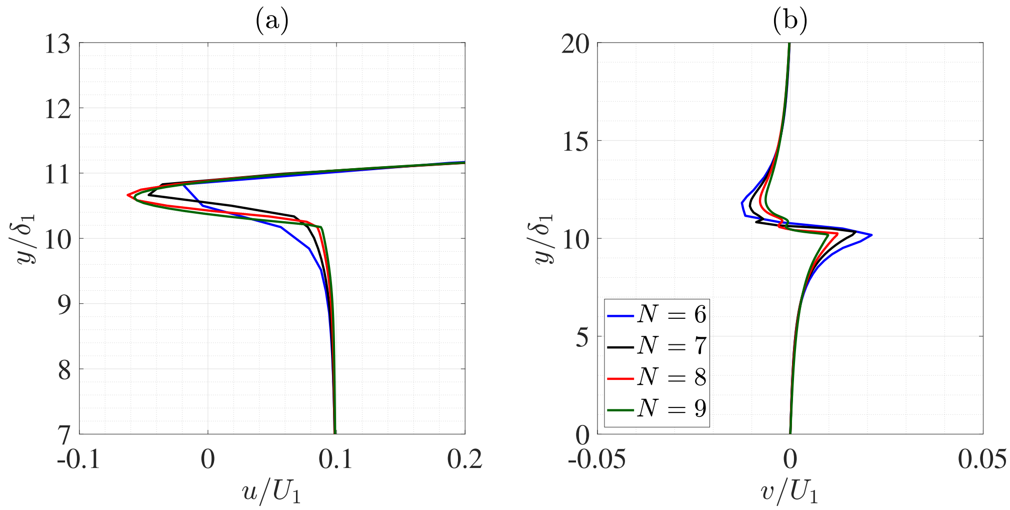

Figure 14: Time-averaged streamwise (a) and normal-to-flow (b) velocity component profiles at the location $x/\delta_1 = 2$ by varying the maximum grid refinement level: $N = 6$ (blue); $N = 7$ (black); $N = 8$ (red); $N = 9$ (green).

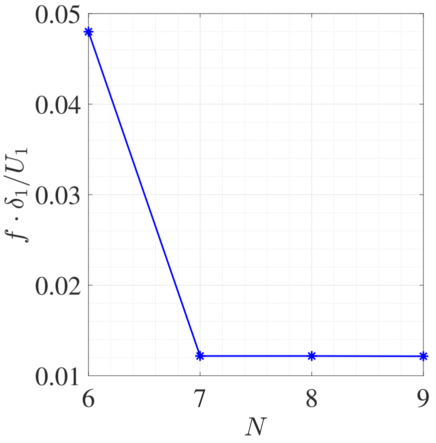

Figure 15: Frequency of the interface oscillation at the location $x/\delta_1 = 8$ by varying the maximum grid refinement level N.

black curves) and fine ($N = 8$, red curves) meshes succeed. Moreover, excellent agreement is observed between the results from the $N = 8$ and $N = 9$ (green curves) meshes. Similar conclusions can be drawn from Fig. 15, which shows the variation in interface oscillation frequency across the four refinement levels at $x/\delta_1 = 8$, where the wavy dynamics are fully developed. Based on this analysis, the computational grid $N = 8$ has been considered sufficient to produce accurate and reliable results for the two-phase flow dynamics, and it has therefore been used for the simulations presented in this work.

References

[1] H. Helmholtz, On discontinuous movements of fluids, The London, Edinburgh, and Dublin Philosophical Magazine and Journal of Science 36 (244) (1868) 337–346.

[2] W. Thomson, Hydrokinetic solutions and observations, The London, Edinburgh, and Dublin Philosophical Magazine and Journal of Science 42 (1871) 362–377.

[3] H. G. Im, B. T. Helenbrook, S. R. Lee, C. K. Law, Ignition in the supersonic hydrogen/air mixing layer with reduced reaction mechanisms, Journal of Fluid Mechanics 322 (1996) 275–296.

[4] A. H. Lefebvre, Atomization and sprays, Emisphere Publishing (1989).

[5] J. Wu, S. Popinet, L. Deike, Revisiting wind wave growth with fully coupled direct numerical simulations, Journal of Fluid Mechanics 951 (2022) A18.

[6] M. Tadros, M. Ventura, C. Guedes Soares, Review of current regulations, available technologies, and future trends in the green shipping industry, Ocean Engineering 280 (2023) 114670.

[7] P. E. Dimotakis, Two-dimensional shear layer entrainment, AIAA Journal 24 (11) (1986) 1791–1796.

[8] P. Marmottant, E. Villermaux, On spray formation, Journal of Fluid Mechanics 498 (2004) 73–111.

[9] Y. Ling, D. Fuster, G. Tryggvason, S. Zaleski, A two-phase mixing layer between parallel gas and liquid streams: multiphase turbulence statistics and influence of interfacial instability, Journal of Fluid Mechanics 859 (2019) 268–307.

[10] J. P. Matas, S. Marty, A. Cartellier, Physics of liquid jets, Reports on Progress in Physics 71 (2008) 036601.

[11] J. P. Matas, S. Marty, A. Cartellier, Experimental and analytical study of the shear instability of a gas-liquid mixing layer, Physics of Fluids 23 (2011) 094112.

[12] P. Yecko, S. Zaleski, J. M. Fullana, Viscous modes in two-phase mixing layers, Physics of Fluids 14 (12) (2005) 4115–4122.

[13] T. Boeck, S. Zaleski, Viscous versus inviscid instability of two-phase mixing layers with continuous velocity profile, Physics of Fluids 17 (2005) 032106.

[14] T. Otto, M. Rossi, T. Boeck, Viscous instability of a sheared liquid-gas interface: dependence on fluid properties and basic velocity profile, Physics of Fluids 25 (2013) 032103.

[15] P. Huerre, P. A. Monkewitz, Local and global instabilities in spatially developing flows, Annual Review of Fluid Mechanics 22 (1) (2005) 473–537.

[16] D. Fuster, J. P. Matas, S. Marty, S. Popinet, J. Hoepffner, A. Cartellier, S. Zaleski, Instability regimes in the primary breakup region of planar coflowing sheets, Journal of Fluid Mechanics 736 (2013) 150–176.

[17] C. Bozonnet, J. P. Matas, G. Balarac, O. Desjardins, Stability of an air-water mixing layer: focus on the confinement effect, Journal of Fluid Mechanics 933 (A14) (2022) 1–27.

[18] J. P. Matas, A. Delon, A. Cartellier, Shear instability of an axisymmetric air-water coaxial jet, Journal of Fluid Mechanics 843 (2018) 575–600.

[19] J. P. Matas, Inviscid versus viscous instability mechanism of an air-water mixing layer, Journal of Fluid Mechanics 768 (2015) 375–387.

[20] M. P. Juniper, The full impulse response of two-dimensional jet/wake flows and implications for confinement, Journal of Fluid Mechanics 590 (2007) 163–185.

[21] M. P. Juniper, O. Tammisola, F. Lundell, The local and global stability of confined planar wakes at intermediate reynolds number, Journal of Fluid Mechanics 686 (2011) 218–238.

[22] J.-P. Matas, Inviscid vs viscous instability mechanism of an air-water mixing layer, Journal of Fluid Mechanics 768 (2015) 375–387.

[23] A. Della Pia, T. Michelis, M. Chiatto, M. Kotsonis, L. de Luca, Global dynamics and topology of two-phase mixing layer flow through simultaneous gas and liquid velocity measurements, Journal of Fluid Mechanics 981 (2024) A13.

[24] B. Rayana, Contribution à l'étude des instabilités interfaciales liquide-gaz en atomisation assistée et taille des gouttes, PhD thesis (2007).

[25] F. Ben Rayana, A. Cartellier, E. Hopfinger, Assisted atomization of a liquid layer: investigation of the parameters affecting the mean drop size prediction, Proceedings of the International Conference on Liquid Atomization and Spray Systems (ICLASS), Kyoto, Japan. (2006) 375–387.

[26] R. Scardovelli, S. Zaleski, Direct numerical simulation of free-surface and interfacial flow, Annual Review of Fluid Mechanics 31 (1) (1999) 567–603.

[27] S. Popinet, Gerris: a tree-based adaptive solver for the incompressible Euler equations in complex geometries, Journal of Computational Physics 190 (2) (2003) 572–600.

[28] D. Fuster, A. Baguè, T. Boeck, A. Le Moyne, L. Leboissetier, S. Popinet, P. Ray, R. Scardovelli, S. Zaleski, Simulation of primary atomization with an octree adaptive mesh refinement and vof method, International Journal of Multiphase Flow 35 (2009) 550–565.

[29] A. Baguè, D. Fuster, S. Popinet, R. Scardovelli, S. Zaleski, Instability growth rate of two-phase mixing layers from a linear eigenvalue problem and an initial value problem, Physics of Fluids 22 (9) (2010) 092104.

[30] A. Arote, M. Bade, J. Banerjee, On coherent structures of spatially oscillating planar liquid jet developing in a quiescent atmosphere, Physics of Fluids 32 (2020) 082111.

[31] A. Liu, D. Sun, B. Yu, J. Wei, Z. Cao, An adaptive coupled volume-of-fluid and level set method based on unstructured grids, Physics of Fluids 33 (2021) 012102.

[32] J. A. van Hooft, S. Popinet, C. C. van Heerwaarden, S. J. A. van der Linden, S. R. de Roode, B. J. H. van de Wiel, Towards adaptive grids for atmospheric boundary-layer simulations, Boundary-Layer Meteorology 167 (3) (2018) 421–443.

[33] M. M. Francois, S. J. Cummins, E. D. Dendy, D. B. Kothe, J. M. Sicilian, M. W. Williams, A balanced-force algorithm for continuous and sharp interfacial surface tension models within a volume tracking framework, Journal of Computational Physics 213 (1) (2006) 141–173.

[34] S. Popinet, An accurate adaptive solver for surface-tension-driven interfacial flows, Journal of Computational Physics 228 (16) (2009) 5838–5866.

[35] S. Osher, J. A. Sethian, Fronts propagating with curvature-dependent speed: Algorithms based on hamilton-jacobi formulations, Journal of Computational Physics 79 (1988) 12–49.

[36] M. Sussman, P. Smereka, S. Osher, A level set approach for computing solutions to incompressible two-phase flow, Journal of Computational Physics 114 (1994) 146–159.

[37] S. O. Unverdi, G. Tryggvason, A front-tracking method for viscous, incompressible, multi-fluid flows, Journal of Computational Physics 100 (1992) 25–37.

[38] G. Tryggvason, B. Bunner, A. Esmaeeli, D. Juric, N. Al-Rawahi, W. Tauber, J. Han, S. Nas, Y.-J. Jan, A front-tracking method for the computations of multiphase flow, Journal of Computational Physics 169 (2001) 708–759.

[39] D. Jacqmin, Calculation of two-phase navier–stokes flows using phase-field modeling, Journal of Computational Physics 155 (1999) 96–127.

[40] J. Kim, Phase-field models for multi-component fluid flows, Communications in Computational Physics 12 (3) (2005) 613–661.

[41] S. Elghobashi, On predicting particle-laden turbulent flows, Applied Scientific Research 52 (1994) 309–329.

[42] S. Balachandar, J. K. Eaton, Turbulent dispersed multiphase flow, Annual Review of Fluid Mechanics 42 (2010) 111–133.

[43] J. J. Monaghan, Simulating free surface flows with sph, Journal of Computational Physics 110 (1994) 399–406.

[44] M. Ishii, T. Hibiki, Thermo-Fluid Dynamics of Two-Phase Flow, Springer, 2011.

[45] R. T. Lahey, D. A. Drew, The Analysis of Two-Phase Flow, American Nuclear Society, 2005.

[46] X. Shan, H. Chen, Lattice boltzmann model for simulating flows with multiple phases and components, Physical Review E 47 (1993) 1815–1819.

[47] S. Succi, The Lattice Boltzmann Equation for Fluid Dynamics and Beyond, Oxford University Press, 2001.

[48] P. J. Schmid, Dynamic mode decomposition of numerical and experimental data, Journal of Fluid Mechanics 656 (2010) 5–28.

[49] F. Andreuzzi, N. Demo, G. Rozza, A dynamic mode decomposition extension for the forecasting of parametric dynamical systems, SIAM Journal on Applied Dynamical Systems 22 (3) (2023) 2432–2458.

[50] D. C. Giovanni, S. Onofrio, L. Stefano, D. P. Pietro, S. Cherubini, Dynamic-mode-decomposition of the wake of the nrel-5mw wind turbine impinged by a laminar inflow, Renewable Energy 199 (2022) 1–10.

[51] A. Colanera, A. Della Pia, M. Chiatto, Data-driven global stability of vertical planar liquid jets by dynamic mode decomposition on random perturbations, Physics of Fluids 34 (12) (2022) 122101.

[52] B. O. Koopman, Hamiltonian systems and transformation in hilbert space, Proceedings of the National Academy of Sciences 17 (5) (1931) 315–318.

[53] K. Taira, S. Brunton, S. Dawson, C. Rowley, T. Colonius, B. McKeon, O. Schmidt, S. Gordeyev, V. Theofilis, L. Ukeiley, Modal analysis of fluid flows: An overview, AIAA Journal 55 (2017).

[54] J. H. Tu, C. W. Rowley, D. M. Luchtenburg, S. L. Brunton, J. N. Kutz, On dynamic mode decomposition: Theory and applications, Journal of Computational Dynamics 1 (2) (2014) 391–421.

[55] B. F. Armaly, F. Durst, J. C. F. Pereira, B. Schonung, Experimental and theoretical investigation of backward-facing step flow, Journal of Fluid Mechanics 127 (1983) 473–496.

[56] F. Rumsey, T. Mccormick, Sound and recording: An introduction (5th edition), Routledge (2009).

[57] C. H. K. Williamson, Vortex dynamics in the cylinder wake, Annual Review of Fluid Mechanics 28 (1996) 477–539.

[58] B. R. Noack, K. Afanasiev, M. Morzyński, G. Tadmor, F. Thiele, A hierarchy of low-dimensional models for the transient and post-transient cylinder wake, Journal of Fluid Mechanics 497 (2003) 335–363.

[59] J. L. Proctor, S. L. Brunton, J. N. Kutz, Dynamic mode decomposition with control, SIAM Journal on Applied Dynamical Systems 15 (1) (2016) 142–161.

[60] M. Cenedese, J. Axås, B. Bäuerlein, K. Avila, G. Haller, Data-driven modeling and prediction of non-linearizable dynamics via spectral submanifolds, Nature Communications 872 (2022).